Spectral Indices for Estimating Exposed Carbonate Rock Fraction in Karst Areas of Southwest China

Xiangjian Xie, Peijun Du, *Senior Member, IEEE*, Junshi Xia, and Jieqiong Luo

***Abstract*—The quantitative estimation of the fractional cover of carbonate rock (CR) is critical for natural resource management and ecological conservation in karst areas. Based on the analysis of spectral properties of CR together with other land cover types, we proposed two CR indices (CRIs) and established the model that represents the relationships between the CRIs and the fractional cover of CR. Then, the fractional cover of CR was estimated by using the developed model. Experimental results on Landsat-8 Operational Land Imager images acquired at Southwestern China demonstrated the effectiveness of the developed model. Compared with other indices, the proposed CRIs show the highest correlations with the fractional cover of CR.**

***Index Terms*—Carbonate rock indices (CRIs), fractional cover, karst ecosystem, Landsat Data Continuity Mission (LDCM) Operational Land Imager (OLI), remote sensing, spectral index.**

I. Introduction

KARST landscape covers about 15% of the Earth's surface and spans significant areas of Asia, Europe, and the America. The karst mountain region of Southwestern China, one of the largest karst geomorphology regions, is viewed as one of the most serious regions undergoing environmental degradation in China [1], [2]. Karst rocky desertification (KRD), as one of the most serious problems in land degradation, occurs and develops quickly under the impact of anthropogenic activities [3]. KRD is closely related to the distribution of pure or mixed carbonate rock (CR). In KRD areas, the most obvious land-surface symptoms are the exposure of CR and low vegetation cover [4]. Therefore, the estimation of exposed CR fractional cover is essential for karst ecological conservation and environmental management.

Remote sensing techniques provide an important way for understanding karst environment. In recent years, remotely sensed data have been applied extensively to monitor karst environment in large geographic areas. The traditional way of estimating land cover fractions and land degradation in karst areas is to do either site investigations or visual interpretation of satellite images [5]. However, it is very time consuming, labor intensive, and susceptible to the interpreter's bias. In order to accurately estimate land cover fractions in karst areas, particularly at subpixel scale, spectral mixture analysis (SMA) and spectral indices are often used. For instance, Yue *et al.* segmented an Advanced Spaceborne Thermal Emission and Reflection Radiometer (ASTER) image into relatively homogeneous subsets and then estimated the photosynthetic vegetation using a normalized difference vegetation index spectral mixture analysis (NDVI-SMA) model [6]. Although the SMA algorithms are physical based approaches and able to acquire subpixel endmember fractions effectively [7], [8], it is extremely difficult to be applied in a large geographic area for practical users because of the difficulties in endmember selection and intraclass variability quantification, etc.

Compared with the SMA method, spectral indices have apparent advantages due to their easy implementation and convenience in practical applications. The most popular one applied in karst environment may be the karst rocky desertification synthesis index (KRDSI) [5]. Although this index has been proven effective to a certain degree, it suffers a serious limitation. KRDSI, which derived from narrow shortwave infrared bands (2000–2400 nm), is only deployed on hyperspectral images. Narrow shortwave infrared bands are generally not available on low-cost multispectral sensors. Therefore, it is in urgent need to develop effective spectral indices in order to satisfy the demands of multispectral remote sensing imagery. In this letter, we proposed two carbonate rock indices (CRIs) to meet the demand. Furthermore, we also developed a model to quantitatively estimate the fractional cover of multispectral imagery.

The remainder of this letter is organized as follows. Section II describes the study area and data sets. The proposed CRIs and the developed model are presented in Section III. Section IV illustrates the experimental results of this letter. Conclusions are drawn in Section V at last.

II. Study Area and Data Sets

The study area is a karst peak-cluster depression region in northeastern Jianshui County, located 133 km southeast of Kunming City, Yunnan Province, China. The fields used

Manuscript received January 31, 2015; revised March 20, 2015 and May 25, 2015; accepted May 29, 2015. Date of publication June 15, 2015; date of current version August 7, 2015. This work was supported by the China Geological Survey Project under Grant 12120113007500. *(Corresponding author: Peijun Du.)*

X. Xie, P. Du, and J. Luo are with the Key Laboratory for Satellite Mapping Technology and Applications of National Administration of Surveying, Mapping and Geoinformation of China, Beijing 100830, China, and also with the Jiangsu Provincial Key Laboratory of Geographic Information Science and Technology, Nanjing University, Nanjing 210093, China. They are also partly affiliated with Jiangsu Center for Collaborative Innovation in Geographical Information Resource Development and Application, Nanjing 210023, China (e-mail: xiexjrs@gmail.com; dupjrs@gmail.com; luojq_rs@126.com).

J. Xia is with the Key Laboratory for Satellite Mapping Technology and Applications of National Administration of Surveying, Mapping and Geoinformation of China, Nanjing 210023, China, and with the Jiangsu Provincial Key Laboratory of Geographic Information Science and Technology, Nanjing University, Nanjing 210093, China, and also with UMR 5218-IMS-Laboratoire de l'Intégration du Matériau au Système, University of Bordeaux, 33405 Talence, France. He is also partly affiliated with Jiangsu Center for Collaborative Innovation in Geographical Information Resource Development and Application (e-mail: xiajunshi@gamil.com).

Color versions of one or more of the figures in this paper are available online at http://ieeexplore.ieee.org.

Digital Object Identifier 10.1109/LGRS.2015.2441962

TABLE I
LANDSAT-8 OLI SPECTRAL BANDS

Spectral	Band Wavelength	Resolution
Band 1 - Coastal/Aerosol	433 - 453 nm	30 m
Band 2 - Blue	450-515 nm	30 m
Band 3 - Green	525-600 nm	30 m
Band 4 - Red	630-680nm	30 m
Band 5 - Near Infrared	845-885 nm	30 m
Band 6 - Short Wavelength Infrared	1560-1660 nm	30 m
Band 7 - Short Wavelength Infrared	2100-2300 nm	30 m
Band 8 - Panchromatic	500-680 nm	15 m

for validation purposes were located on $23°48'33.49'' - 23°48'39.12''$ N and $103°0'24.87'' - 103°7'54.70''$ E with an area of 162.56 km^2. The main biophysical compositions of the karst surface include the following: bare bedrock (CR), soils, and green vegetation. Bare bedrock is the dominant land cover, followed by dry land and nature vegetation areas.

An LDCM (also referred to as Landsat 8) Operational Land Imager (OLI) image (path 129, row 44) acquired on April 23, 2014 was employed in this study. The spectral bands of Landsat-8 OLI can be detailed in Table I. The OLI image was corrected radiometrically using the relative spectral response filters and the radiometric calibration coefficients delivered with the data [9]. The reflectance was then calculated via The Environment for Visualizing Images (ENVI) Fast Line-of-sight Atmospheric Analysis of Hypercubes (FLAASH) tools. In order to guarantee more pure pixels of rock, soils, or vegetation, the Gram–Schmidt spectral sharpening algorithm implemented in ENVI software [10] was employed to enhance the spatial resolution of spectral rectified OLI bands 1–7 (30-m spatial resolution), using panchromatic band 8 (15-m spatial resolution).

III. METHODOLOGY

The main steps of estimating exposed CR fraction in karst areas can be summarized as follows:

1) selecting pure samples;
2) analyzing the spectral reflective characteristic of CR associated with other land cover types;
3) proposing two CRIs;
4) developing the model that represents the relationships between the CRIs and the fractional cover of CR;
5) applying the model to produce the full map of the fractional cover in the study area.

In the first step, with the help of the high spatial resolution image (acquired on February 5, 2014) provided by Google Earth, 68 pure pixels (approximately 10–15 pixels per class) were selected from the multispectral image to calculate the mean reflectance of five typical land cover types (CR, soil, vegetation, sheds, and water) in the study area. Fig. 1 shows the reflectance of typical land covers.

In the study area, vegetation, soil, and CR are the three main land cover types. In the following, we focus on analyzing spectral properties of the three land cover types.

According to the second national soil survey data, the karst areas of Southwestern China is dominated by red loam, latosolic red loam, and yellow loam, which contain a large number of hematite and goethite [11]. The spectrum of hematite

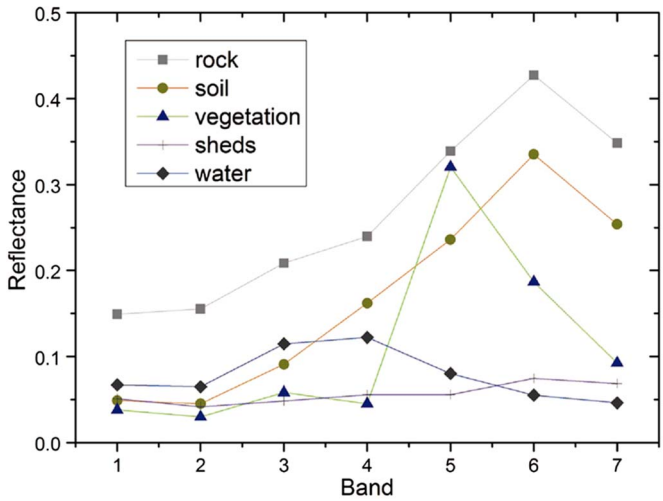

Fig. 1. Reflectance spectra of each typical land cover (CR, soil, vegetation, sheds, and water) in karst area.

$(\alpha - Fe_2O_3)$ is characterized by high and nearly constant reflectivity at longer wavelengths in the visible and near infra-red (VIS-NIR), a reflectivity minimum near 880 nm, a shoulder centered near 620 nm, and a band with very low reflectivity near 510 nm. The reflectivity of goethite $(\alpha - FeOOH)$ is relatively high at longer wavelengths in the VIS-NIR region from the absorption band that occurs near 930 nm. The other three absorption bands for goethite are near 660, 480, and 420 nm, respectively [12], [13]. For the aforementioned reasons, soil has the lowest reflectivity in band 1 (433–453 nm) and band 2 (450–515 nm) in the Landsat-8 OLI image, while the marginalized absorption in the NIR band (845–885 nm) is not obvious because of the broadband, resulting in a steep slope between band 2 and band 5 (seen in Fig. 1).

The spectral reflectance curve of vegetation has a significant minimum of reflectance in the visible portion of the electromagnetic spectrum because the main pigment, chlorophyll, strongly absorbs the blue (450 nm) and red (670 nm) bands. Beyond visible wavelengths (longer than 700 nm), the spectra of fresh plants show a strong rise in reflectance, which resulted from an increased amount of light scattering at cell-wall interfaces because of a change in the index of refraction. The aforementioned chemical composition and physical properties of vegetation can be indicated distinctly on the plot (see Fig. 1). For the CR, there would be very few absorptions in the VIS-NIR region. In this case, the combination of blue and near-infrared bands can help identify CR and other types. To be specific, compared with soil and vegetation, CR shows the higher values of the ratio between the blue and near-infrared bands. Therefore, it is possible to define some indices related to estimate CR by using the blue and near-infrared bands.

Based on the analysis of spectral signatures of CR, soil, and vegetation in the second step, we proposed two CRIs under the ratio and normalized difference forms in the third step, which can be defined as follows:

$$CRI1 = \rho_{\text{blue}}/\rho_{NIR} \tag{1}$$

$$CRI2 = \frac{\rho_{\text{blue}} - \rho_{NIR}}{\rho_{\text{blue}} + \rho_{NIR}} \tag{2}$$

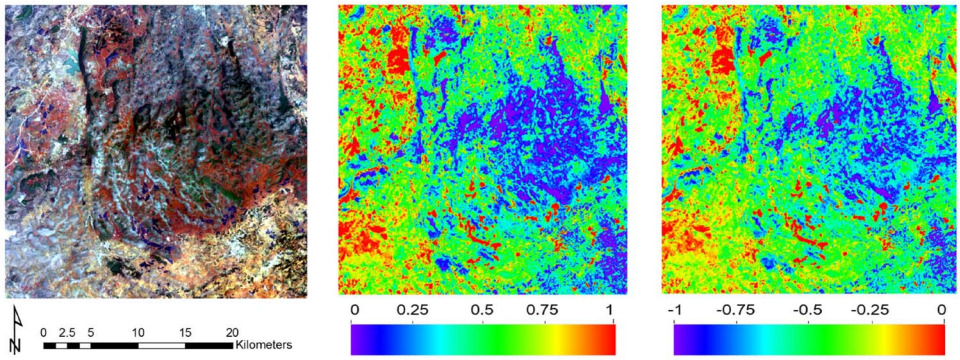

Fig. 2. Spatial distribution of CRIs derived from the Landsat-8 OLI image in the study area. (a) True color composite image (R:4, G:3, B:2). (b) Map of CRI1. (c) Map of CRI2.

TABLE II
MAXIMUM, MINIMUM, AND MEAN VALUES OF CR, SOIL, AND GREEN IN CRI IMAGES

Land cover types	CRI1			CRI2		
	Max	Min	Mean	Max	Min	Mean
CR	**0.45**	**0.41**	**0.43**	**-0.38**	**-0.42**	**-0.40**
Vegetation	0.13	0.10	0.04	-0.77	-0.91	-0.83
Soil	0.24	0.13	0.18	-0.61	-0.77	-0.69

where ρ_{blue} and ρ_{NIR} are the spectral reflectances of blue and near-infrared bands, respectively. With the increase of CR, the ratio or normalized difference between the blue and near-infrared bands will be larger, but lower for vegetation or soil in karst areas.

In the fourth step, in order to effectively estimate exposed CR fraction in a karst environment, a linear model is constructed to represent the relationship between CRIs and CR fraction. Although the linear model has already been used to express the relationships between vegetation/impervious surface indices and vegetation/impervious surface fraction [14]–[16], to the best of our knowledge, it has not been investigated in a karst area using multispectral remote sensing images. For this purpose, the high spatial resolution image provided by Google Earth used in the first step was applied to a real CR fraction image. First, we resampled the Landsat-8 OLI image into a spatial resolution of 90 m, with the intent to get more mixed pixels at a larger scale level. CRI images were also calculated by using the proposed CRIs. Then, 100 pixels are randomly selected from the CRI maps and also converted into square cells in Environmental Systems Research Institute (ESRI) Shapefile format. These square cells were inserted in Google Earth, and ground-truth information of CR fractions was then obtained by visual interpretation. Eight pixels that cover water or sheds of pseudoginseng were removed, and the remaining 92 pixels were used in the model. The linear model is defined as follows:

$$f = a + b \times CRIs \tag{3}$$

where f is the fraction of exposed CR and a and b are estimated parameters. It is expected that CRIs will have a very strong linear correlation with the "ground-truth" fractions of CR.

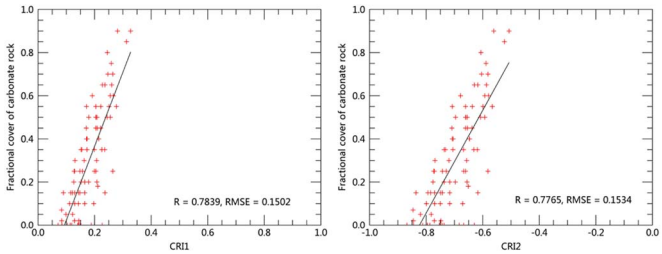

Fig. 3. Relationships between the proposed CRIs and the fractional cover of CR. (a) Relationship between CRI1 and the fraction of CR. (b) Relationship between CRI2 and the fraction of CR.

TABLE III
CROSS-VALIDATION: MEANS OF R AND RMSE OF THE LINEAR MODELS DERIVED FROM THE RELATIONSHIPS BETWEEN SOME INDICES AND CR FRACTIONS

Model	Numerator	Denominator	RMSE	R
CRI1	Blue	NIR	**0.150**	**0.784**
CRI2	Blue	NIR	0.153	0.777
Ratio	Blue	Green	0.166	0.735
Normailize	Blue	Green	0.169	0.724
Normailize	Blue	SWIR1	0.180	0.674
Ratio	Blue	SWIR1	0.182	0.669
Ratio	Green	NIR	0.181	0.667
Normailize	Green	NIR	0.184	0.660
Normailize	Green	SWIR1	0.209	0.527
Ratio	Green	SWIR1	0.210	0.518
Normailize	Blue	Red	0.222	0.431
Ratio	Blue	SWIR2	0.225	0.413
Normailize	Blue	Red	0.224	0.399
Ratio	Blue	SWIR2	0.229	0.381
Normailize	SWIR1	SWIR2	0.228	-0.369
NDRI	SWIR1	Red	0.236	-0.334
NDVI	NIR	Red	0.234	-0.325

After the parameters of a and b are determined, the full map of the fractional cover of CR can be estimated by the model with the proposed CRIs.

IV. EXPERIMENTAL RESULTS AND ANALYSIS

In this section, experimental results on a Landsat-8 OLI image acquired in the Jianshui County of Yunnan (Southwestern China) are presented.

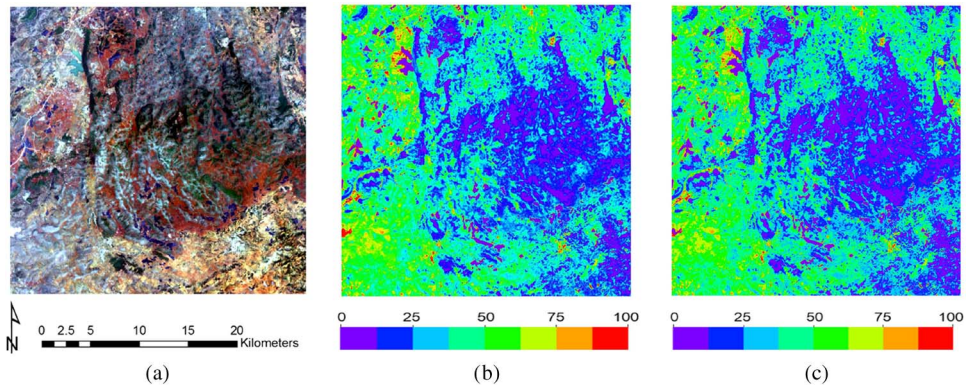

Fig. 4. Fraction images of the developed models with the proposed CRIs. (a) True color composite image (R:4, G:3, B:2). (b) Fraction image of the developed model with CRI1. (c) Fraction image of the developed model with CRI2.

The CRI images derived from the Landsat-8 OLI image are illustrated in Fig. 2. The value range of CRI1 and CRI2 are from 0 to 1 and -1 to 0, respectively. From the two figures, it can be seen that water and sheds of pseudoginseng have the highest values, followed by gray buildings and roads composed of concrete or asphalt. However, they are not main land cover types in karst areas and easy to be extracted. As mentioned previously, vegetation, soil, and CR are the three main land cover types. Table II lists the maximum, minimum, and mean values of CR, soil, and green in CRI images using the pure samples. It can be found in this table that CR has greater values than vegetation and soil. Among them, vegetation has the lowest values. In summary, the CRI1 and CRI2 images show strong separability between CR and other land cover types, including soil and vegetation, which maybe benefit to estimate the fraction of CR in the next step.

In order to estimate the exposed CR fraction in a karst area, a linear model is constructed to represent the relationships between CRIs and CR fraction. Correlation analysis was used to examine the model. In particular, Pearson (R) and root-mean-square error (RMSE) are adopted as the quantitative indicators. R is a measure of the linear correlation (dependence) between two variables, giving a value between $+1$ and -1 inclusive, where 1 is total positive correlation, 0 is no correlation, and -1 is total negative correlation. Moreover, lower values of RMSE indicate the better model. In order to evaluate various predictive models, a tenfold cross-validation framework was introduced and did ten runs, and the ten results were averaged to produce an estimation at last. Fig. 3 presents the relationships between the proposed CRIs and the fractional cover of CR. For CRI1, R and RMSE are 0.7839 and 0.1502, respectively. For CRI2, R and RMSE are 0.7765 and 0.1534, respectively. They indicated that the proposed CRIs show strong relationships with the fractional cover of CR. Therefore, it can be used to estimate the fraction of CR.

In addition, in order to illustrate the effectiveness of the proposed CRIs, several ratio or normalized indices calculated by two optional OLI bands were added as the comparisons. Table III gives the result of ten tenfold cross-validation runs: means of R and RMSE of the linear models (the best 15 models, normalized difference rock index (NDRI) and NDVI sorted in descending order of R) derived from the relationships between other indices and CR fraction. From Table III, we can find that the proposed CRIs show the strongest relationships with the fractional cover of CR and have the lower values of RMSE. Although the joint use of NDVI and NDRI is considered to be useful for discriminating karst rock and nonkarst rock in [17], their correlation with the fractional cover of CR is not significant. For NDRI, R and RMSE are -0.3343 and 0.2360, respectively. For NDVI, R and RMSE are 0.3254 and 0.2339, respectively. Overall, the proposed spectral indices (CRI1 and CRI2) can be effectively used to estimate the fractional cover of CR in karst areas.

The developed models based on the proposed CRIs can be expressed as follows:

$$f = -0.320 + 3.429 \times CR1 \tag{4}$$

$$f = 1.960 + 2.379 \times CR2. \tag{5}$$

Fraction images of the developed models via the proposed CRIs are presented in Fig. 4. Compared with the true color composite image [see Fig. 3(a)], the CR can be well estimated with high values of the fraction. The fraction results obtained from CRIs which were derived from Landsat-8 OLI imagery support the hypothesis that the fractions of CR might be resolved within the blue and NIR bands. The smaller the slope of the reflectance curve of soil and vegetation between 450 and 850 nm, the greater the fraction of CR. In order to test the robustness of the developed models, two test experiments with different study areas using two Landsat OLI image scenes were done, respectively. One is located on $23°29'58.72'' - 23°36'1.25''$ N, $102°36'55.38'' - 102°43'26.58''$ E, and the other one is located on $23°47'58.05'' - 23°59'24.75''$ N, $103°46'6.56'' - 103°57'40.57''$ E. As described in Section II, the two study areas have the similar landscape condition to the aforementioned one (i.e., the main bare land, dry land, and vegetation areas). To evaluate the proposed models presented in (4) and (5), 85 pixels and 74 pixels were randomly selected in the two study areas. The following table (see Table IV) gives the predicted RMSEs of the learned models in two scenes. As shown in Table IV, the proposed models share the top position in two scenes. For instance, the proposed CRIs have the lowest values of RMSE (0.206 and 0.205, respectively) for the second scene. For the first scene, the combination of green and SWIR1 performed

TABLE IV
PREDICTED RMSE OF THE LEARNED LINEAR MODELS IN TWO OTHER DIFFERENT SCENES

Model	Numerator	Denominator	RMSE (scene1)	R (scene1)	RMSE (scene2)	R (scene2)
CRI1	Blue	NIR	0.198	**0.750**	0.206	**0.746**
CRI2	Blue	NIR	0.199	0.747	**0.205**	0.732
Ratio	Blue	Green	0.208	0.677	0.226	0.660
Normailize	Blue	Green	0.206	0.683	0.220	0.655
Normailize	Blue	SWIR1	0.278	0.621	0.224	0.655
Ratio	Blue	SWIR1	0.267	0.621	0.223	0.635
Ratio	Green	NIR	0.275	0.640	0.221	0.560
Normailize	Green	NIR	0.265	0.628	0.219	0.551
Normailize	Green	SWIR1	0.195	0.749	0.246	0.683
Ratio	Green	SWIR1	**0.193**	0.747	0.246	0.688
Normailize	Blue	Red	0.221	0.609	0.244	0.524
Ratio	Blue	SWIR2	0.216	0.680	0.209	0.580
Normailize	Blue	Red	0.223	0.582	0.229	0.508
Ratio	Blue	SWIR2	0.218	0.674	0.243	0.572
Normailize	SWIR1	SWIR2	0.254	-0.214	0.230	-0.183
NDRI	SWIR1	Red	0.251	-0.164	0.213	-0.179
NDVI	NIR	Red	0.261	-0.100	0.243	-0.089

well, even better than the proposed models on RMSE and R, which may be due to the contribution of buildings, some of which are made up of CR. In summary, the proposed CRIs are effective in discriminating CR and soil (vegetation), and the developed models can be used to respectively estimate the fractional cover of CR in the different typical karst areas of Southwest China.

V. CONCLUSION

In this letter, two CRIs for quantitatively estimating the fraction of CR in a karst peak-cluster depression area were developed. The theoretical basis for the method relies in combining the spectral feature observed in CR, soils, and vegetation at 450–880 nm. It was found that CR could be effectively resolved from the Landsat-8 OLI image by combining blue (Band 2) and NIR (Band 5) bands. Furthermore, a linear model was constructed to represent the relationships between the CRIs and the fractional cover of CR. R and RMSE measures in correlation analysis were used to examine the models. The results demonstrate that the proposed CRIs perform better in estimating the fractional cover of CR in karst areas. By using the developed models, the fractional cover of CR can be effectively estimated in a karst environment with a large geographic area. In future studies, we will focus on developing the enhanced CRIs with three bands.

REFERENCES

[1] Y. Jiang, L. Li, C. Groves, D. Yuan, and P. Kambesis, "Relationships between rocky desertification and spatial pattern of land use in typical karst area, southwest China," *Environ. Earth Sci.*, vol. 59, no. 4, pp. 881–890, 2009.

[2] P. Zhang *et al.*, "Rocky desertification risk zone delineation in karst plateau area: A case study in Puding county, Guizhou province," *Chin. Geographical Sci.*, vol. 20, no. 1, pp. 84–90, 2010.

[3] D. Yuan, "Modern karstology and global change study," *Earth Sci. Frontiers*, vol. 4, no. 1/2, pp. 17–25, 1997.

[4] S.-J. Wang, Q.-M. Liu, and D.-F. Zhang, "Karst rocky desertification in southwestern China: Geomorphology, land use, impact and rehabilitation," *Land Degradation Develop.*, vol. 15, no. 2, pp. 115–121, 2004.

[5] Y. Yue *et al.*, "Spectral indices for estimating ecological indicators of karst rocky desertification," *Int. J. Remote Sens.*, vol. 31, no. 8, pp. 2115–2122, 2010.

[6] Y. Yue *et al.*, "Development of new remote sensing methods for mapping green vegetation and exposed bedrock fractions within heterogeneous landscapes," *Int. J. Remote Sens.*, vol. 34, no. 14, pp. 5136–5153, 2013.

[7] R. L. Powell, D. A. Roberts, P. E. Dennison, and L. L. Hess, "Sub-pixel mapping of urban land cover using multiple endmember spectral mixture analysis: Manaus, Brazil," *Remote Sens. Environ.*, vol. 106, no. 2, pp. 253–267, 2007.

[8] J. Franke, D. A. Roberts, K. Halligan, and G. Menz, "Hierarchical multiple endmember spectral mixture analysis (MESMA) of hyperspectral imagery for urban environments," *Remote Sens. Environ.*, vol. 113, no. 8, pp. 1712–1723, 2009.

[9] J. R. Irons, J. L. Dwyer, and J. A. Barsi, "The next Landsat satellite: The Landsat data continuity mission," *Remote Sens. Environ.*, vol. 122, pp. 11–21, 2012.

[10] C. A. Laben and B. V. Brower, "Process for enhancing the spatial resolution of multispectral imagery using pan-sharpening," US Patent 6 011 875, Jan. 4, 2000.

[11] G. Fischer *et al.*, "Global agro-ecological zones assessment for agriculture," IIASA, Laxenburg, Austria and FAO, Rome, Italy, Tech. Rep. IR-00-064, 2008.

[12] J. L. Mortimore, L.-J. R. Marshall, M. J. Almond, P. Hollins, and W. Matthews, "Analysis of red and yellow ochre samples from clearwell caves and Çatalhoyuk by vibrational spectroscopy and other techniques," *Spectrochimica Acta Part A: Mol. Biomolecular Spectroscopy*, vol. 60, no. 5, pp. 1179–1188, 2004.

[13] B. Stenberg, R. A. V. Rossel, A. M. Mouazen, and J. Wetterlind, *Chapter Five-Visible and Near Infrared Spectroscopy in Soil Science*, ser. Advances in Agronomy, D. L. Sparks, Ed. New York, NY, USA: Academic, 2010, vol. 107, pp. 163–215.

[14] G. Gutman and A. Ignatov, "The derivation of the green vegetation fraction from NOAA/AVHRR data for use in numerical weather prediction models," *Int. J. Remote Sens.*, vol. 19, no. 8, pp. 1533–1543, 1998.

[15] K. Wittich and O. Hansing, "Area-averaged vegetative cover fraction estimated from satellite data," *Int. J. Biometeorol.*, vol. 38, no. 4, pp. 209–215, 1995.

[16] M. E. Bauer, C. L. Brian, and W. Bruce, " Estimating and Mapping Impervious Surface Area by Regression Analysis of Landsat Imagery, " in *Remote Sensing of Impervious Surfaces* G.Stefani, Eds. Boca Raton, FL, USA: Taylor & Francis, 2008, pp. 3–19.

[17] Q. Huang and Y. Cai, "Mapping karst rock in southwest china," *Mountain Res. Develop.*, vol. 29, no. 1, pp. 14–20, 2009.